X-ray CT imaging of 3-D bearing capacity mechanism for vertically loaded shallow foundations

D. Takano[1],J. Otani[2],M. Nakamura[3], and R. Mokwa[4]
[1]*Geotechnical Engineering Division, Port and Airport Research Institute, Yokosuka, Japan*
[2]*X-Earth center, KumamotoUniversity, Kumamoto, Japan*
[3]*Sumitomo Mitsui Construction Co., Ltd. (formerly at KumamotoUniversity), Tokyo, Japan*
[4]*MontanaStateUniversity, College of Engineering, Bozeman, Montana*
E-mail: takano-d@pari.go.jp

ABSTRACT: The three-dimensional bearing capacity of shallow foundations has not been fully investigated because of the difficulty in visualizing and understanding the complex three-dimensional failure mechanism. In this paper, a series of model loading tests were conducted on shallow foundations with square and rectangular shaped footings X-ray CT scanning techniques were utilized to nondestructively visualize and investigate the soil behavior during the loading tests. Based on the tomographic results for four different footing geometries, both surface deformations and below ground deformations along the failure surface cross section are described and three-the dimensional failure mechanisms illustrated. A gradual change or progression of the bearing capacity failure pattern was observed and quantified as the footing aspect ratio changed from a square foundation to a rectangular shape that approached plane strain conditions. It is anticipated that the process and technique developed in this study could be beneficial in understanding and quantifying the mechanics associated with other soil-structure interaction problems, especially complex problems in which the failure mechanism is difficult or impossible to predict using conventional geotechnical engineering principles.

1. INTRODUCTION

The plane strain bearing capacity failure mechanism for shallow strip foundations has been well documented in the literature; for example, Lamb and Whitman (1979) and Yamaguchi *et al*. (1976). However, the bearing capacity failure mechanism of foundations with finite shapes such as square- or rectangular-shaped foundation bases have many uncertainties and have not been investigated in a thorough and rationale approach because of the complexities in evaluating and experimentally modeling three-dimensional (3-D) failure zones (Okamura *et al*.1993, Liu et al. 2007, Ueno 1998). Bearing capacity calculation methods are available in which empirical factors are used to account for different shapes of foundation bases (Meyerhof 1963, Japan Road Association 2003). These shape factors are categorized as experimental approximations rather than theoretically accurate adjustments, because the factors were determined based on the gross behavior of model and full scale tests on idealized soils (De Beer *et al*. 1970).Only limited studies have been conducted that systematically evaluate the 3-D bearing capacity mechanism of shallow foundations (Lyamin *et al*. 2006, Narita *et al*. 1992).

The objective of this paper is to qualitatively and quantitatively investigate the 3-D bearing capacity mechanism of shallow foundations with different shapes of the footing base. A series of model loading tests were conducted using dry sandy soil with different sizes and shapes of shallow foundations. An industrial X-ray CT scanner was used to examine and quantify deformations and strains within the loaded soil mass as the footings were loaded. The authors have conducted previous studies using X-ray CT in geotechnical engineering applications and have validated that this technology is useful for visualizing soil behavior and soil response nondestructively; i.e., without introducing testing or measurement bias (Otani *et al*. 2000, Otani *et al*. 2005, Otani *et al*. 2006, Chevalier *et al*. 2011 and Watanabe *et al*. 2012).

The results of this experimental study and analysis are described herein, as follows: 1) shallow foundation model load testing apparatus; 2) application of X-ray CT to the experimental and analytical phases of the test program; 3) implications and observations regarding soil behavior and the bearing capacity mechanism and 4) the bearing capacity of vertically loaded shallow foundations with square or rectangular shaped footing bases is verified using experimentally verified, measured data.

2. OUTLINE OF MODEL LOADING TEST

2.1 Test Apparatus

A hollow cylindrical soil box with an inner diameter of 300mm was used in this test. The soil box was constructed of an acrylic material that is transparent to x-ray penetration. The total height of the soil model was 200mm. The foundation soil consisted of dry Toyoura sand prepared by air pluviation. A target relative density, D_r of 90% was achieved in all tests and is indicative of a very dense condition for the foundation soils around the model footings. The properties of Toyoura sand are summarized in Table 1 and a schematic view of the test apparatus is shown in Figure 1.

Table 1 Property of Toyoura Sand

ρ_s (g/cm^3)	ρ_{dmax} (g/cm^3)	ρ_{dmin} (g/cm^3)	D_{50} (mm)	U_c
2.656	1.645	1.333	0.160	1.50

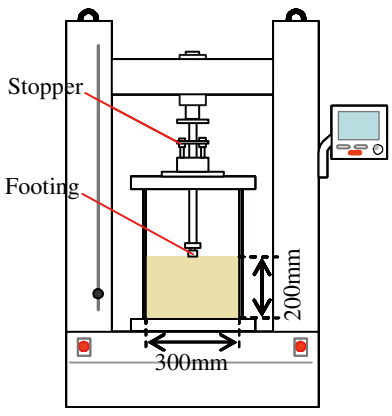

Figure 1 Schematic view of experimental set-up

The vertical load was applied using a specially constructed attachment that prevented moment loadings and ensured the loading plate was applied vertically and concentrically. The loading was periodically stopped using a temporary locking mechanism (labeled 'stopper' in Fig. 1) to remove the soil box for X-ray CT scanning. The loading plates were used to model rectangular or square footing foundations, as shown in Table 2 and Photo 1. The footings in three of the test cases had constant cross-section areas of 1600 mm^2, with different ratios of short and long sides (B:L = 1:1 for Case 1, 1:1.5 for Case 2 and 1:2 for Case 3). Case 1 represents a square footing shape while Case 2 and Case 3 represent rectangular-shaped footings. Case 4 (B:L = 1:4) simulated the condition of plane strain and was conducted for comparative purpose. The area of the foundation base for Case 4 was two times larger than the footing areas for the other cases. The foundation bases were covered with sand paper to ensure a fully frictional failure mode. The load was applied by a standard loading apparatus using a displacement controlled speed set at a vertical travel rate of 0.1 mm/min.

Table 2 Size of model foundations

	Width of short side: B (mm)	Width of long side: L (mm)	Area of base (mm^2)	Short-to-long ratio (B:L)
Case 1	40.00	40.00		1:1
Case 2	32.65	49.00	1600	1:1.5
Case 3	28.30	56.55		1:2
Case 4	28.30	113.10	3200	1:4

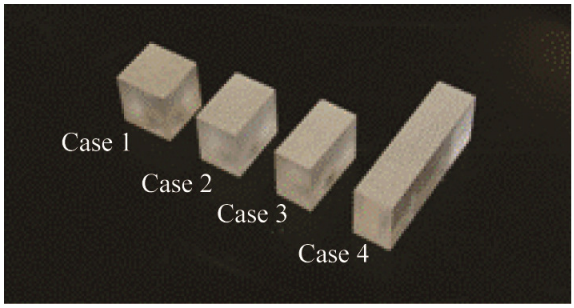

Photo 1 View of model foundations

2.2 Stress-Settlement Relationship

Figure 2 shows the results of stress-settlement relationship for all the cases. The applied stress was used for these comparisons, instead of piston load, because axial stress provided a logical metric for normalizing the effect of different foundation base areas with respect to applied load. As shown in Fig. 2, a peak value of stress occurred near an approximate vertical settlement of 3 mm for all the cases, including the plane strain condition (Case 4). The peak stress levels for Case 1, Case2 and Case3 are in close agreement (less than 4% variation), while the peak of the stress-settlement curve for Case 4 is considerably larger (about 60%) than the other cases. This difference in peak value for Case 4 can partially be attributed to boundary condition effects, in which the size of the long side of the rectangular base is relatively close to the sides of the soil box for this test configuration. As shown in Fig. 2, the stress levels in each case decrease after the peak and appear to asymptotically approach residual conditions at larger settlements. The value of stress corresponding to residual conditions varies between the cases. Interestingly, regardless of the footing aspect ratio, the peak value of stress occurs at a relatively early stage of foundation movement (vertical settlement) followed by a rapid decrease of stress to residual stress values, which appear to be directly correlated to the footing aspect ratio.

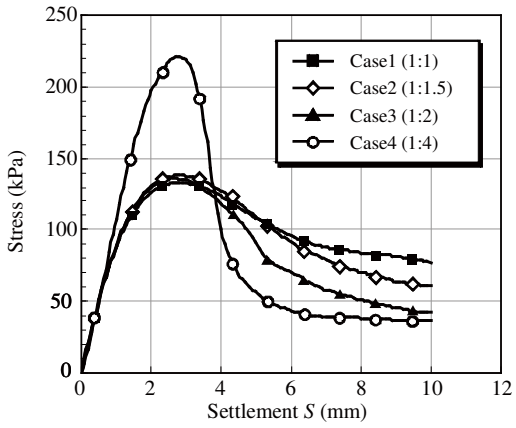

Figure 2 Measured vertical stress-ground settlement curve

3. X-RAY CT

3.1 Relationship between CT-value and Soil Density

Tomographic studies on geomaterials conducted during the past two decades indicate that X-ray CT technology provides a viable means for nondestructively observing, measuring and quantifying the internal microstructure of geomaterials. X-rays that penetrate an object will encounter an X-ray sensitive screen within the CT apparatus and cause it to illuminate. During X-ray exposure, the object's matter will absorb some of the X-rays and the intensity (energy per unit area per unit time) of the X-ray will attenuate as it is absorbed and scattered by the atoms of the material X-ray computed tomography utilizes a back analysis procedure to obtain the spatial distribution of absorbed X-rays obtained from multiple projections of the scanned object (Otani *et al*. 2000 and Otani 2003). The degree of absorption is related to material density by the CT-value, which is an integral part of image processing analyses. The CT-value is commonly defined by the following equation:

$$CT\text{-}value = K(\mu_t - \mu_w)/\mu_w \quad (1)$$

Where μ_t= coefficient of X-ray absorption for the material; μ_w= coefficient of X-ray absorption for water, and K=a constant in which a value of 1000 was used in this study. Figure 3 shows the relationship between CT-value and the density of a range of materials, including: air, water, acrylic and Toyoura sand. The shaded vertical band that is shown in this figure brackets the range of measured dry density for Toyoura sand. As shown in Fig. 3, the relationship between density and CT-value is well correlated, indicating material density can be accurately estimated from CT results developed in this study. In this paper, the soil density value, which is more significant for practical considerations, will be used in most of the evaluations in place of the tomographic CT-value.

3.2 CT Images

After a sample is scanned, the recorded data is assimilated into a digital representation using computer-based algorithms. Converting recorded X-ray data into a digital image is one of the primary functions of computed tomography. A reconstructed tomographic data file provides a quantifiable description of solid particles and void spaces in a series of two-dimensional (2-D) cross-sectional images, which also can be combined together to create a 3-D volume view of the scanned object (Alramahi and Alshibli 2006). Each pixel of a scanned image represents the average density of a voxel (volumetric representation of a pixel) at a particular (x, y) location. Acomplete 3-D image is constructed by assembling the large number of voxels, which can then be used to quantify solid particulate distributions, void space distributions and 3-D geometric measurements.

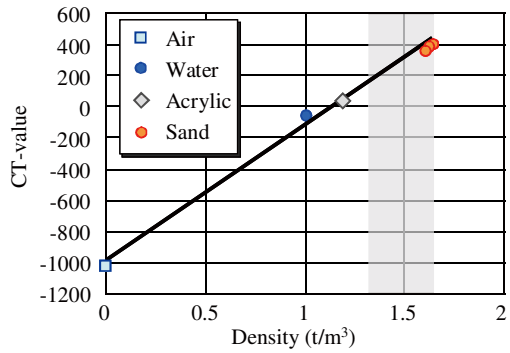

Figure 3 Calibration of CT-value against known density of materials

An industrial X-ray CT device located at Kumamoto University was used to scan the 400 mm diameter load testing apparatus that was used to model the foundation conditions. The total voxel data set size was 2048 x 2048, which resulted in an individual voxel size of 0.1953 x 0.1953 x 2.00 mm^3, as shown in Figure 4.The CT-value and density within a voxel depend on the ratio between the size of a particle and the size of the voxels used in the analysis (Otani *et al.* 2005). A smoothing technique, called the Median filter, was used for 11 x 11 voxels to filter and reduce noise in the CT results.

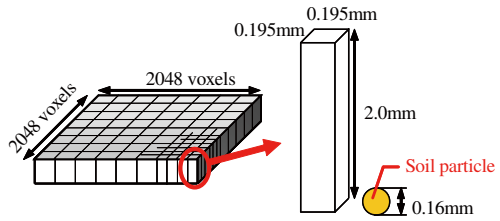

Figure 4 Comparison between the size of a voxel and a soil particle

A graphical comparison between voxel size and the average particle size of Toyoura sand is shown in Fig. 4. Based on a relative comparison between average soil particle size and the CT voxel size, it was reasonable to assume that the CT-value is representative of the sand total density; but, the CT-value does not necessarily provide a consistently reliable estimate of the specific density of each individual particle.

A useful aspect of CT analyses is that the size, shape and location of shear band development along failure margins can be quantified on the voxel level in which low density regions represent local shear zones. Close examination of the reconstructed CT images in this study shows clear evidence of shear band development in the sand failure mass during footing loading. The CT data indicates that when the initial relative density of the ground is relatively high, similar to the test conditions of this research, positive dilatancy occurs along the shear band due to localized expansion of void space. This can be observed in the CT images as low density zones concentrated in narrow regions along the shear band, as shown in Figure 5. In general, the width of the shear band was measured to be approximately 10 to 20 times the average size of soil particles, which agrees with previous measurements by Tatstuoka *et al.* (1991).

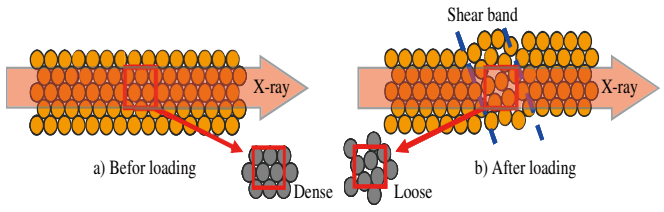

Figure 5 Illustration of shearing on dense ground composed of single grain size

4. EVALUATION OF THE 3-D BEARING CAPACITY MECHANISM

4.1 CT Images and Density Change

Figure 6 shows cross sectional CT images corresponding to a foundation settlement of 10mm for all test cases. Each row of the figure shows horizontal cuts (2-D CT slices) at five different locations beneath the footing base at depths of 5, 15, 25, 25 and 45mm. Figure 7 provides additional CT images that show vertical cross sectional cuts (slices) taken through the center of each footing. The slice images are oriented parallel to both the long side (L-dimension) and the short side (B-dimension) of the footings. (The long and short sides for the square footing, Case 1, are the same; i.e., B = L.) Six gray scales of gradation shading were used in Fig. 6 to visually represent different levels of density ranging from 1.10 to 1.83 t/m^3. In Fig. 7, a continuous gradation of colors was used to represent different values of density within the soil mass in order to make the zones of low density more readily apparent. The darker shades of gray in the CT images of Fig. 6 and Fig. 7 represent areas of relatively low density and the lighter gray shades represent higher density locations. The areas of total black color with square and rectangular shapes in the leftmost column of the images (5mm depth) in Fig.6 represent the footings, which were constructed of an acrylic material whose density (1.19 t/m^3) is relatively lower than the density of soil that was used in the model. The darker gray shades in the soil mass represent low density zones or bands indicative of strain localizations. In the horizontal cross-sections (Fig 6) the highly strained areas appear as thin lines tracing the approximate shape of an oblate spheroid. In the vertical cross-section view (Fig. 7), the strain localization trace appears to match quite closely the shape of the theoretical failure surface initially proposed by Karl Terzaghi (1943) approximately 70 years ago.

Figure 8 shows the variation of density distribution along a longitudinal cross section beneath the Case 3 footing, which is shown in the 2-D CT slice in Fig. 8(a). Figure8(b) shows the profile of ground density for Case 3 along line A-B, which was drawn diametrically through the center of a horizontal slice at a depth of 15mm, as shown in Fig.8(a).The data from these tests show that the soil density directly beneath the footing remains relatively unchanged after loading. This zone represents an active earth pressure region. Moreover, close inspection of Fig. 8(b) shows two additional low density regions, which are : 1) low density regions directly surrounding the active earth pressure zones and 2) a thin low density area that is relatively far removed. This zone is located about 25mm left of the centerline shown in Fig. 8(a). These two low density regions represent the transient region (also called the Prandtl radial shear zone) and the frictional failure surface from the theory of bearing capacity.

These zones of strain localization are readily apparent in the cross-section CT scans shown in Fig. 7.The vertical cross-section images for Case 1 indicate that for a square-shaped footing, the failure zones appear nearly the same in the two orthogonal views (i.e., parallel to the B and L dimensions). The two side views indicate a symmetrical density distribution during loading of the square footing with a similar failure mechanism including active earth pressure (high density), transient (relatively low density), and passive earth pressure (high density) zones. It is also interesting to note that the area of the tip of active earth pressure zone (apex of the theoretical triangle) for Case 1 is not precisely defined in the images; however, lower density areas are clearly apparent on both sides of the triangular active zone. For the cases of rectangular footings (Case 2, Case 3 and Case 4), the theoretical triangular-shaped active earth pressure zone appears in the short side cross-section view (parallel to the B-dimension) for all the rectangular footings. The results shown in the Fig. 7 CT images are in good agreement with the conventional bearing capacity mechanism proposed by Terzaghi (1943) for the short side of the foundation, which is consistent with the bearing capacity equation that has been used in practice for many years. These observations indicate that the failure surface is disproportionately formed on the short side of the

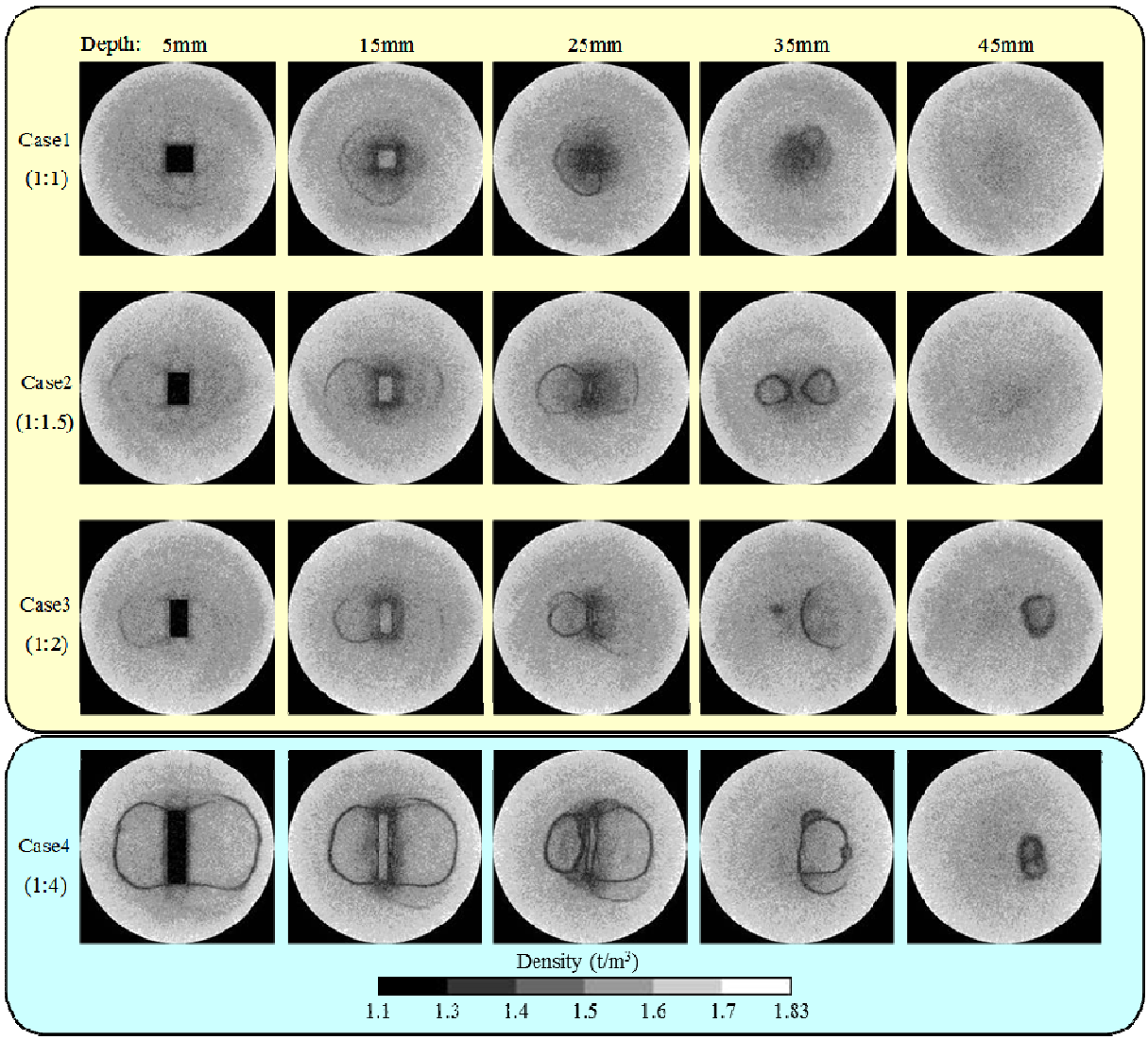

Figure 6 Horizontal cross-section of CT image (distribution of ground density on horizontal cross-section)

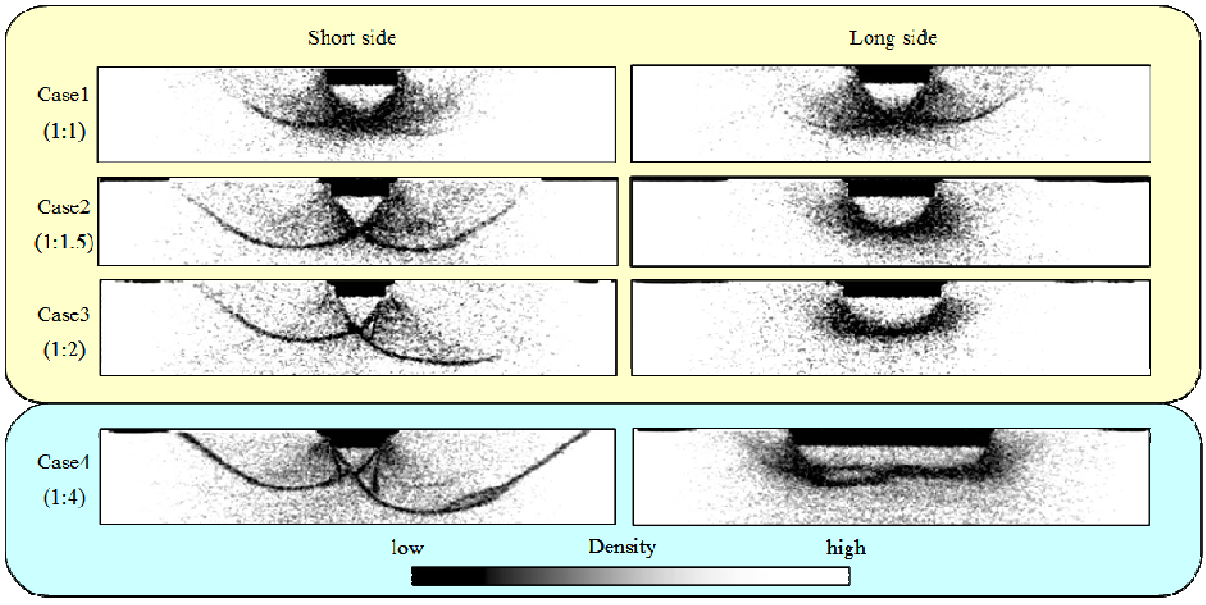

Figure 7 Vertical cross-section of CT image (distribution of ground density on vertical cross-section)

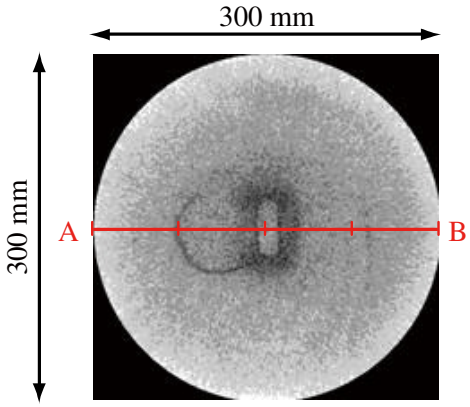

(a) 2D CT slice

angle, $\alpha_2 = \pi/4 - \varphi/2$) and plastic zone. The depth of this mechanism, H_1 is defined by following equation:

$$H_1 = Be^{(\pi/2)\tan\varphi/2} \quad (2)$$

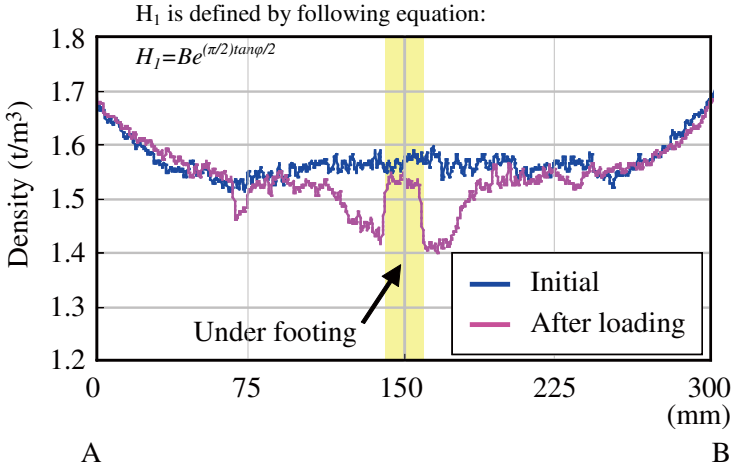

(b) Profile of ground density

Figure 8 Distribution of ground density at 15mm of depth in Case 3 (B: L=1:3)

footing (parallel to the B-dimension) and the failure mechanism can be modeled reliably as a 2-D failure surface for rectangular and continuous footings. CT imaging also shows that areas of strain localization coincide with changes of density as a result of dilation and compressive changes within the failure mass. Dilation and void ratio increase is a representative response for very dense granular material and compression of void space generally occurs in nondense granular materials and nearly all soils at high strain levels.

Figure 9 shows views of 3-Dimages extracted from the X-ray CT scans during foundation loading. The degree of shading illustrates changes that occur in the soil density as loading progresses for each of the four cases. The low density zone in Case 1 is a good example of an axisymmetric failure pattern. It can be observed in the cases of the rectangular shaped foundations (Case 2, Case 3 and Case 4) that the shape of the low density areas vary as a function of the long side of the footing (L-dimension) and the L/B aspect ratio. It is also evident that the low density failure plane extends deeper and spreads laterally wider as the footing aspect ratio increases.

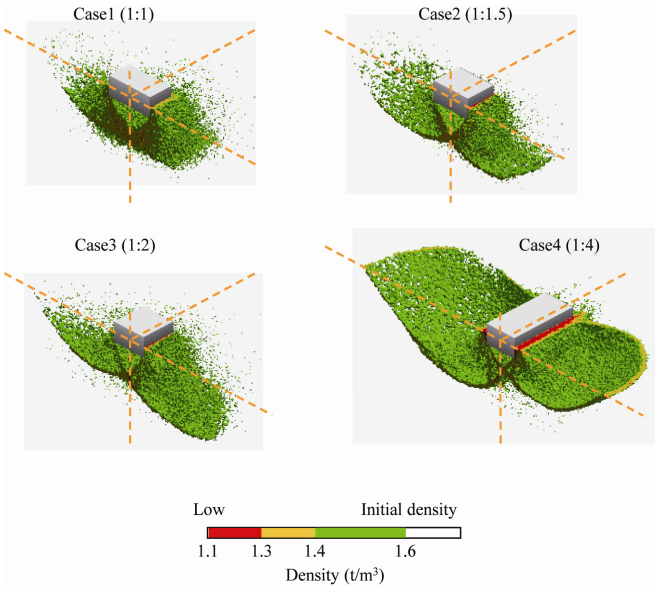

Figure 9 3D extraction of low density zone

4.2 Discussion on Bearing Capacity Theory

Figure 10 shows the well-known 2-D bearing capacity failure mechanism proposed by Terzaghi (1943), which consists of an active wedge (active wedge angle, α_1), passive zone (passive wedge

Table 3 summarizes a comparison between CT measured, back-calculated values and values calculated directly from Terzaghi's bearing capacity theory; column I versus column II, respectively. The angle of the active wedge, α_1, and the width of the slip surface, W_1, was measured directly from the CT images. The active wedge angle, α_1 was measured as the angle between the base of foundation and the line segment that forms the outer boundary of the triangular active zone, as shown in Fig. 10. The width of the slip surface (W_1) was measured as the length between the corner of the footing and the outer extension of the slip surface as it emerges at the ground surface. The angle of the active wedge and the width of the slip surface were measured at both ends of the footing and, in some cases, the measured values varied slightly. The values presented in Table 3 represent the mean of the measurements obtained parallel to both the short and the long sides of the footings.

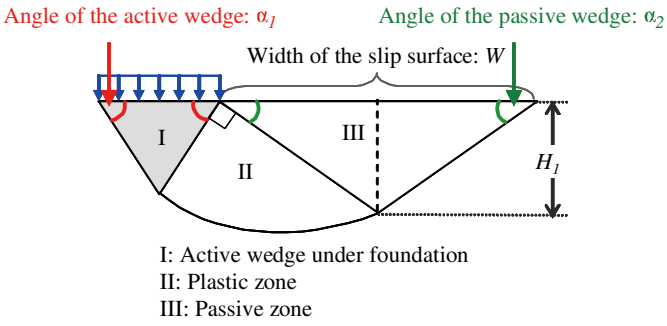

Figure 10 Shape of the slip surface based on Terzaghi's bearing capacity theory

Table 3 Angle of the active wedge and width of the slip surface;
(I) shows measured results from CT images and
(II) shows calculated results by Terzaghi's bearing capacity theory

		(I)			(II)		
	Direction	α_1	$W_1(mm)$	W_1/B	φ	$W_2(mm)$	W_2/B
Case1(1:1)	Short	45.21	67.06	1.68	0.42	40.76	1.02
	Long	45.55	70.00	1.75	1.09	42.01	1.05
Case2(1:1.5)	Short	52.25	91.18	2.79	14.5	63.30	1.94
	Long	54.93	60.00	1.22	19.85	81.98	1.67
Case3(1:2)	Short	58.53	101.2	3.58	27.06	103.2	3.64
	Long	57.41	66.47	1.18	24.81	91.49	1.62

The results shown in Table 3 indicate that the angle of the active wedge, α_1 tends to increase with increase in aspect ratio (L/B); consequently, α_1 is not just a function of the friction angle, as traditionally assumed. For aspect ratios approaching 1.0 (Case 1, square footing), the angle α_1 approaches 45 deg, which is consistent with Terzaghi's (1943) original assumption for continuous footings (plane strain condition).In other words, the test results indicate that when the true 3-D bearing capacity failure pattern is considered, the angle of the active wedge is not a constant parameter as defined by 2-D bearing capacity theory. For each case, the angle of the active wedge was equivalent whether it was measured parallel or perpendicular to the short footing side. This indicates, as shown in Figure 11, that the shape of the active wedge that develops beneath square footings takes the shape of an inverted symmetrical triangular prism, while the active zone beneath a rectangular footing takes the polyhedral shape of an inverted triangular prism that is extended (stretched) in the direction of the footing's long dimension.

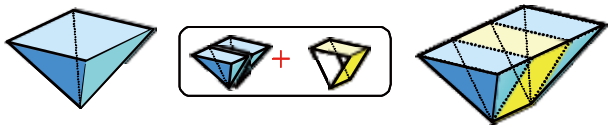

a) Square b) Rectangle

Figure 11 Illustration of 3D shape of the active wedge

For plain strain conditions, the long dimension (L-dimension) of the prism extends to infinity. The width of slip surface measured from CT images, W_1 in Table 3, gradually increases with respect to the aspect ratio when measured parallel to the B dimension of the footing. In contrast, the dimension W_1 decreases with respect to aspect ratio when measured parallel to the L dimension. The theoretically calculated width of slip surface, W_2, shows relatively smaller values than measured : however, this discrepancy between experimental measurement and theoretical value becomes smaller as the aspect ratio increases toward plane strain conditions.

Figure 12 shows the change of internal friction angle back-calculated from measured values of the angle α_1 for the different cases evaluated in this study. The four cases are represented in the plot in terms of their respective aspect ratios (L/B). The dashed line represents a smooth curve fitted to the data points. The internal friction angle was back-calculated from α_1 measured in the CT images using the relationship accredited to Vesic (1973), in which $\alpha_1=\pi/4+\varphi/2$. As shown in Figure 12, the relationship between the back-calculated friction angle and the footing shape function (i.e., aspect ratio, L/B)indicates that as the aspect ratio approaches the plane strain condition (high L/B ratio), the back-calculated internal friction angle converges to the friction angle measured by laboratory testing, which ranged from 40 to 45 deg. This observation appears logical and reasonable based on bearing capacity theory and Vesic's (1973) experiments; however, the observation is based on extrapolation of the test results and requires additional experimentation to more fully investigate this relationship.

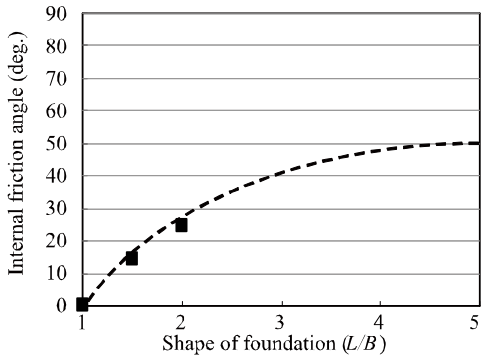

Figure 12 Change of the internal friction angle calculated from CT-image

The unrealistic values of the friction angle displayed in Fig. 12 indicate that the true expression for α_1 is between $\{\pi/4\}$ (Terzaghi 1943) and $\{\pi/4+\varphi/2\}$ (Vesic 1973). For the soil conditions tested in this study, Terzaghi's (1943) relationship appears most applicable for small L/B ratios, while for larger L/B ratios, Vesics (1973) approximation for α_1 is more accurate.

It can be ascertained from observations of the CT images and based on calculations and geometric measurements, that the relationship between the active wedge geometry and the internal friction angle gradually approach the expression $\{\alpha_1= \pi/4+\varphi/2\}$ as the shape of the footing approaches the plane strain condition, or as the rectangular footing aspect ratio increases to values of L/B ~> 3.0. Interestingly, for a square footing (L/B = 1.0) the active wedge geometry is more accurately portrayed using Terzaghi's original approximation of ($\alpha_1 = \pi/4$). Terzaghi applied this approximation to the plane strain condition; although, the tests conducted in this study indicate this approximation ($\alpha_1 = \pi/4$) is relatively accurate for square-shaped footings, while Vesic's approximation ($\alpha_1 = \pi/4+\varphi/2$) is more appropriate for continuous footings and for rectangular footings with high aspect ratios. These tests illustrate the continual progressive change in the failure zone as the footing shape changes from square, to rectangular, to the plane strain condition.

5. CONCLUSIONS

The bearing capacity failure mechanism for square and rectangular shaped shallow foundations was investigated using X-ray CT technology in conjunction with model footing loading tests. This investigation represents an original detailed study in which the 3-D bearing capacity failure mechanism is qualitatively and quantitatively evaluated using nondestructive experimental techniques. Conclusions drawn from this study are summarized as follows:

(1) The bearing capacity mechanism of shallow foundations were visualized and analyzed for the first time using X-ray CT.

(2) The use of X-ray CT made the examination of soil behavior during loading possible and the mechanism of bearing capacity failure and accompanying shear zones for shallow foundations were clearly observed and evaluated.

(3) There is a variation in the size and shape of the shear zone and failure surface as viewed from the two primary orthogonal planes (i.e., parallel to the L-dimension versus parallel to the B-dimension) for rectangular footings.

(4) Footings with larger aspect ratios (approaching a continuous or strip foundation), exhibited failure patterns similar to the theoretical plane strain condition when the failure surface is observed parallel to the footing B-dimension. In this case, the active failure wedge is accurately defined by the corner angle $\alpha_1 = \pi/4+\varphi/2$. For square footings, the active failure wedge is more accurately defined by the angle $\alpha_1 = \pi/4$.

(5) This study showed there is a gradual change or progression of the bearing capacity failure pattern as the footing aspect ratio changes from 1.0 (square foundation) to rectangular shaped footings with relatively large L/B ratios.

6. REFERENCES

Alramahi, B. and K. Alshibli. (2006) "Applications of CT to characterize the internal structure of geomaterials: limitations and challenges." ASCE Geotechnical Special Publication No. 149, Site and Geomaterial Characterization, Shanghai, China, pp. 88-95.

Chevalier, B. and Otani, J. (2011) "Arching observation in three-dimensional trapdoor problem with X-ray CT and discrete element method", Soils and Foundations, Vol.51, No.3, pp. 459-469.

De Beer, E. E. (1970) "Experimental determination of the shape factors and the bearing capacity factors of sand".Geotechnique, Vol. 20, No. 4, pp. 387-411.

Japan Road Association. (2003) "Specifications for highway bridges" Maruzen Co. Ltd.

Lamb, T. W. and Whitman, R. V. (1979) "Soil Mechanics, SI Version". JOHN WILEY & SONS Publishing Company, Ch.4, New York.

Liu, Y., Sreng, S., Mochizuki, A., Ueno, K. and Tsuboi, Y. (2007) "Bearing capacity tests under 1g and 20g field of shallow foundation on dense sand and their deformation behaviours". Japanese Geotechnical Journal, Vol. 2, No. 3, pp. 139-148 (in Japanese).

Lyamin, A.V., Salgado, R., Sloan, S.W. and Preszzi, M. (2006): Two- and Three-Dimensional Bearing Capacity of Footings in Sand, Personal communication with Prof. Salgado.

Meyerhof, G.G. (1963) "Some recent research on the bearing capacity of foundations." Canadian Geotechnical Journal, Vol. 1, No. 1, pp. 16-26.

Narita, K., Yamaguchi, H. (1992) "Three-dimensional bearing capacity analysis of foundations by use of amethod of slices." Soils and Foundations, Vol.32, No.4, pp. 143-155.

Okamura, M., Takemura, J. and Kimura, T. (1993) "A study on bearing capacities of shallow footings on sand". Proceedings of the Japan Society of Civil Engineers, No. 463, III-22, pp. 85-94 (in Japanese).

Otani, J. Mukunoki, T., Obara, Y. (2000) "Application of X-ray CT method for characterization of failure in soils", Soils and Foundations, Vol.40, No.2, pp.111-118.

Otani, J. (2003) "State of the art report on geotechnical X-ray CT research at Kumamoto University", Keynote Lecture, X-ray CT for Geomaterials, Balkema, pp. 43-77.

Otani, J., Mukunoki, T., Sugawara, K. (2005) "Evaluation of particle crushing in soils using X-ray CT data", Soils and Foundations, Vol.45, No.1, pp.99-108.

Otani, J., Pham, K.D., Sano, J. (2006) "Investigation of failure in sand due to laterally loaded pileusing X-ray CT", Soils and Foundations, Vol.46, No.4, pp.529-535.

Tatsuoka, F., et al. (1991) "Progressive failure and particle size effect in bearing capacity of a footing on sand", Proceedings of Geotechnical Engineering Congress, ASCE, Vol.2, pp.788-802.

Terzaghi, K. (1943) "Theoretical Soil Mechanics", John Willeyand sons.

Ueno, K, Miura, K., and Maeda, Y. (1998) "Prediction of ultimate bearing capacity of surface footings with regard to size effects." Soils and Foundations, Vol.38, No.3, pp. 165-178.

Yamaguchi, H., Kimura, T. and Fuji-i, N. (1976) "On theinfluence of progressive failure on the bearing capacity of shallow foundations in dense sand", Soils and Foundations, Vol. 16, No. 4, pp. 11-22.

Vesic, A.S. (1973) "Analysis of ultimate loads of shallow foundations." Journal of the Soil Mechanics and Foundations Division, American Society of Engineers, Vol. 99, No. SM1, pp. 45-73.

Watanabe, Y., Lenoir, N., Otani, J. and Nakai, T. (2012) "Displacement in sand under triaxial compression by tracking soil particles on X-ray CT data.", Soils and Foundations, Vol.52, No.2, pp. 312-320.